ChemSusChem

Research Article
doi.org/10.1002/cssc.202200008

Chemistry Europe
European Chemical
Societies Publishing

www.chemsuschem.org

Metal-Doped PdH(111) Catalysts for CO$_2$ Reduction

Changzhi Ai,[a] Tejs Vegge,[a] and Heine Anton Hansen*[a]

PdH-based catalysts hold promise for both CO$_2$ reduction to CO and the hydrogen evolution reaction. Density functional theory is used to systematically screen for stability, activity, and selectivity of transition metal dopants in PdH. The transition metal elements Sc, Ti, V, Cr, Mn, Fe, Co, Ni, Cu, Zn, Y, Zr, Nb, Mo, Ru, Rh, Ag, Cd, Hf, Ta, W, and Re are doped into PdH(111) surface with six different doping configurations: single, dimer, triangle, parallelogram, island, and overlayer. We find that several dopants, such as Ti and Nb, have excellent predicted catalytic activity and CO$_2$ selectivity compared to the pure PdH hydride. In addition, they display good stability due to their negative doping formation energy. The improved performance can be assigned to reaction intermediates forming two bonds consisting of one C—Metal and one O—Metal bond on the PdH surface, which break the scaling relations of intermediates, and thus have stronger HOCO* binding facilitating CO$_2$ activation.

Introduction

Emission of the greenhouse gas carbon dioxide (CO$_2$) has increased rapidly with the development of industrialization in the past decades. A long-term goal of the Paris Agreement was proposed to achieve a balance between CO$_2$ emissions from the combustion of traditional fossil fuels and removals of the greenhouse gas, and it is urgent to limit global warming to 1.5 °C by the year 2100.[1,2] In order to overcome this challenge, the three strategies of decarbonization, carbon sequestration, and carbon recycling will play crucial roles in mitigating net CO2 emissions.[2] The CO$_2$ utilization technology of the electrochemical CO$_2$ reduction reaction (CO$_2$RR) is considered as a promising strategy to convert CO$_2$ into valuable chemicals as it is not only beneficial to carbon recycling but also conducive to increasing chemical energy storage.[3] So far, significant efforts have been made to reduce CO$_2$ to C$_1$–C$_3$ products including formic acid (HCOOH),[4] carbon monoxide (CO),[5] methane (CH$_4$),[6] ethylene (C$_2$H$_4$),[7] methylglyoxal (C$_3$H$_4$O$_2$),[8] acetaldehyde,[9] and alcohols.[10] Among them, CO is one of the most potential products due to the transfer of only two electrons, which leads to higher energy conversion efficiency compared to other products with more electron transfer.[11] More importantly, the hydrogen evolution reaction (HER) usually occurs together with the electrochemical reduction of CO$_2$, CO, and H$_2$, which are the main components of syngas, can be effectively synthesized into liquid hydrocarbons via the Fischer–Tropsch processes.[11,12] Therefore, CO is an important

feedstock in industry and it could be crucial to explore efficient catalysts for conversion from CO$_2$ to CO.

Many previous studies have been done to study metal catalysts for the CO$_2$RR. Gold (Au),[13,14] silver (Ag),[15,16] and copper (Cu)[17] have been the most widely studied for the electrochemical CO$_2$RR and show good performance for CO production. Au nanoparticles formed from thick Au oxide films were reported to have high selectivity for CO$_2$ reduction to CO at 140 mV overpotential and they kept their activity for no more than 8 h.[18] Kim et al. reported Ag nanoparticles supported on carbon has good Faradaic efficiency and low overpotential.[16] Raciti et al. reported that Cu nanowires produced by electrochemical reduction are highly active and selective for the CO$_2$RR to CO at an overpotential of 0.3 V.[17] However, Au, Ag and Cu cannot tune the desired CO/H$_2$ ratio with high CO$_2$RR catalytic activity.[11,19] In addition, metal-nitrogen-carbon (M—N—C) electrocatalysts with high faradaic efficiencies for CO generation are also popular in the field of CO$_2$RR. Among them, Fe—N—C electrocatalyst shows high selectivity and CO formation activity at low overpotentials (0.3 to 0.5 V). Ni—N—C electrocatalyst exhibits good selectivity and activity at higher overpotentials because it is more favorable toward the HER. Co—N—C electrocatalyst has a lower selectivity for CO throughout the entire potential range.[20] Palladium (Pd) was reported to be a potential candidate catalyst for CO2RR to CO by Gao et al. in 2015.[21] Moreover, Chen et. al. thought the Pd catalyst was more suitable to produce syngas (CO$_2$ and H$_2$) compared to other metals, and that the reason why Pd showed good activity and selectivity in the process of electrochemical CO2RR was the Pd metal catalyst was transformed into palladium hydride (PdH).[11] The formation of PdH would significantly improve Faradaic efficiencies of production of CO and H$_2$. Furthermore, the PdH(111) surface experimentally exhibited higher current density and Faradaic efficiency compared with other crystal surfaces.[11] Subsequently, in order to further improve the performance of PdH, several approaches, such as applying transition metal nitrides as promising supports and using bimetallic catalysts has been explored in recent years.[22]

[a] Dr. C. Ai, Prof. T. Vegge, Prof. H. A. Hansen
Department of Energy Conversion and Storage,
Technical University of Denmark
Anker Engelunds Vej, 2800 Kgs. Lyngby (Denmark)
E-mail: heih@dtu.dk

ChemSusChem

Research Article
doi.org/10.1002/cssc.202200008

Chemistry
Europe
European Chemical
Societies Publishing

In this work, density functional theory (DFT) simulations are performed to study transition metal-doped PdH catalysts. Due to the difficult formation of forming HOCO* on the pure PdH(111), we explore the possibility of lowering the HOCO* formation energy through doping transition metal elements Sc, Ti, V, Cr, Mn, Fe, Co, Ni, Cu, Zn, Y, Zr, Nb, Mo, Ru, Rh, Ag, Cd, Hf, Ta, W, and Re into the PdH(111) surface in different configurations to systematically study their properties. First, the doping formation energies are calculated to illustrate the stability of different doped surfaces. Then, the scaling relations between reaction intermediates, free energy diagrams, and kinetic model were carried out to explore the CO$_2$RR catalytic activities after doping. Finally, selectivity toward CO$_2$RR and HER was also studied to describe the competition between CO$_2$ and H$_2$.

Computational Details

All calculations in this work are carried out with spin-polarized density functional theory simulations using the Vienna ab initio simulation package (VASP, version 5.4)[23–26] and the Atomic Simulation Environment (ASE, version 3.2).[27,28] The effects of exchange and correlation are approximated by using the Bayesian error estimation functional with van der Waals correlation (BEFF–vdW).[29] The ionic cores are treated using the projector augmented wave (PAW) method[30] and the wave functions are expanded in a plane waves basis set. A cutoff energy is set as 400 eV and a Gaussian smearing of 0.05 eV is used for the electronic states. In order to remove the electrostatic dipole-dipole interaction between periodically repeated surface slabs, the dipole correction is used in the direction perpendicular to the slab in all calculations. All calculation processes, data col- lection and analysis are performed in a custom build workflow and a computational database is freely available in the DTU Data Repository.[31]

Bulk PdH is in the rock salt (NaCl) crystal structure and the (111) surface, which is energetically the most stable, is considered in this work. A 3×3 supercell model of the PdH(111) with six bilayers is built and each bilayer consists of one Pd atomic layer and one H atomic layer, where the bottom three bilayers are fixed in their bulk positions during optimization. A 3×3×1 Monkhorst-pack grid[32] of k-points is applied to sample the first Brillouin zone of the PdH(111) slab. The convergence threshold of Hellman–Feynman force is set to 0.01 eV Å^{-1} and the energy convergence criteria on each atom was set to 10^{-6} eV atom^{-1}. A vacuum layer of about 15 Å is adopted in z direction to separate periodic slab images and avoid interactions between them. In order to further improve accuracy, a +0.15 eV correction per C=O is applied for systematic overbinding corrections with the BEEF-vdW functional, +0.15 eV for HOCO* and +0.1 eV for H$_2$.[33,34] For solvent stabilization correction at the water-catalyst interface, −0.25 eV for HOCO* and −0.1 eV for CO* are used in all calculations, respectively.[35] The effects of the electric field at the electrochemical interface of catalysis on the free energy of the adsorbates are ignored in this treatment.

The formation energies of PdH doped with transition metals are calculated according to the following definition:

$$E_{form} = E_{nM-doped} - E_{pure} - n\mu_M + n\mu_{Pd} \tag{1}$$

where $E_{nM-doped}$ denotes the energy of doping the PdH(111) slab with n metal atoms, while pure is the energy of the pure undoped

PdH(111) slab. μ_M and μ_{Pd} represent the chemical potential of doped metal atom and Pd, respectively.

The binding energies E_b of different intermediates in this work are given by the following equation:
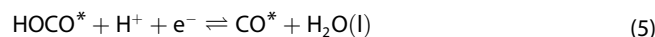
$$E_b = E_{*+intermediate} - E_* - E_{intermediate} \tag{2}$$

where $E_{*+intermediate}$ is the total DFT energy of slab and intermediate. E_* and $E_{intermediate}$ are the energies of clean slab and intermediate with respect to gas phase molecules, respectively.

The calculation of Gibbs free energy (G) is done using Equation (3):

$$G = E_{DFT} + E_{ZPE} + \int C_p dT - TS \tag{3}$$

where E_{DFT} represents the DFT energy with overbinding correction and solvent stabilization correction. E_{ZPE} represents the zero-point energy of the species. C_p and S are the heat capacity and entropy, respectively, and T is temperature. E_{ZPE}, C_p and the entropy of slabs are obtained from statistical mechanics using the harmonic approximation throughout calculations of vibrational frequencies. We assume that variations in these terms are small compared with that of binding energies and thus the energies of these terms for pure PdH(111) are applied to other surfaces as listed in Table S9 in the Supporting Information. Gas-phase species are obtained by ideal gas methods and the corresponding free energies listed in Table S10.

The reaction mechanism for CO$_2$ reduction to CO in this work is considered as follows:[19]

$$CO_2(g) + {}^* + H^+ + e^- \rightleftharpoons HOCO^* \tag{4}$$

$$HOCO^* + H^+ + e^- \rightleftharpoons CO^* + H_2O(l) \tag{5}$$

$$CO^* \rightleftharpoons CO(g) + {}^* \tag{6}$$

Reaction free energies are calculated by the computational hydrogen electrode (CHE) model,[36] which provides an elegant method to avoid calculations of solvated protons. In this model, 0 V is defined based on the reversible hydrogen electrode (RHE). The reaction is defined as in equilibrium at 0 V, at standard pressure:

$$H^+ + e^- \rightarrow 1/2 H_2 \tag{7}$$

Therefore, the sum of the chemical potential of H$^+$ and e$^-$ is equal to half of that of gaseous hydrogen. The reaction free energy dependence on the applied potentials are as follows:

$$\Delta G_1 = G_{HOCO*} - G_* - \mu_{CO_2(g)} - 1/2\mu_{H_2^\ominus} + eU \tag{8}$$

$$\Delta G_2 = G_{CO*} + {}_{H_2O(l)} - G_{HOCO*} - 1/2\mu_{H_2^\ominus} + eU \tag{9}$$

$$\Delta G_3 = G_* + \mu_{CO(g)} - G_{CO*} \tag{10}$$

where the applied potentials are relative to the RHE. ΔG_1, ΔG_2 and ΔG_3 are the free energy difference of the three step reactions for CO$_2$RR. G_{HOCO*}, G_{CO*} and G_* are the free energies of species HOCO*, CO* and the surface, respectively. $\mu_{CO_2(g)}$, $\mu_{CO(g)}$, $\mu_{H_2O(l)}$ and $\mu_{H_2^\ominus}$ represent the chemical potentials of gaseous CO$_2$, gaseous CO, liquid H$_2$O and gaseous H$_2$, respectively.

ChemSusChem

Research Article
doi.org/10.1002/cssc.202200008

**Chemistry
Europe**

European Chemical
Societies Publishing

Moreover, experimental vapor pressures are utilized for them in this work. The partial pressures of H_2O and CO are 3534 Pa and 5562 Pa, respectively.[35] The partial pressure of CO_2 and H_2 are both under standard pressure 101325 Pa.[35,37] We ignore electric field effects on adsorption energies in this work.

The reaction mechanism for the HER can be described by the following steps:[38]

$$H^+ + e^- + * \rightleftharpoons H^* \text{ (Volmer step)} \tag{11}$$

$$H^* + H^+ + e^- \rightleftharpoons H_2(g) + * \text{ (Heyrovsky step)} \tag{12}$$

A kinetic model is utilized to study the activity for CO_2 reduction to CO. The net reaction rates of CO_2RR are described as[39]

$$r_1 = k_1\theta_* p_{CO_2} - \frac{k_1}{K_1}\theta_{HOCO^*} \tag{13}$$

$$r_2 = k_2\theta_{HOCO^*} - \frac{k_2}{K_2}\theta_{CO^*} \tag{14}$$

$$r_3 = k_3\theta_{CO^*} - \frac{k_3}{K_3}\theta_* p_{CO} \tag{15}$$

where k_1, k_2, and k_3 represent forward rate constants for the three steps of CO_2RR. K_1, K_2, and K_3 are the corresponding equilibrium constants and backward rate constants can be calculated by forward rate constant over the corresponding equilibrium constants. For example, backward rate constant is equal to k_1/K_1. p and θ represent the partial pressure and surface coverage, respectively. For the electrochemical step 1 and step 2 with coupled electron proton transfer, the forward rate constants are denoted as

$$k_{i=1,2} = A' exp\left(-\frac{\beta e(U - U_i^0)}{k_B T}\right) \tag{16}$$

where the pre-exponential factor A' is a material independent constant. A value of $A' = 3.6 \times 10^4$ s^{-1} is used as in previous work.[39] k_B is the Boltzmann constant and β is a symmetry factor which is set as 0.5 here. U_i^0 is the reversible potential of reaction step i

$$U_i^0 = -\frac{\Delta G_i}{e} \tag{17}$$

where ΔG_i is the reaction free energy difference at zero voltage (vs. RHE) calculated by DFT using the CHE model. The corresponding equilibrium constants are given by

$$K_i = exp\left(-\frac{e(U - U_i^0)}{k_B T}\right)e \tag{18}$$

For the chemical step 3 with no electron or proton transfer, the rate constant is approximated as

$$k_3 = \nu exp\left(-\frac{E_{CO^*}}{k_B T}\right) \tag{19}$$

where E_{CO^*} represents the binding energy of intermediate CO*. A typical pre-exponential factor ν is 10^{13} s^{-1}.
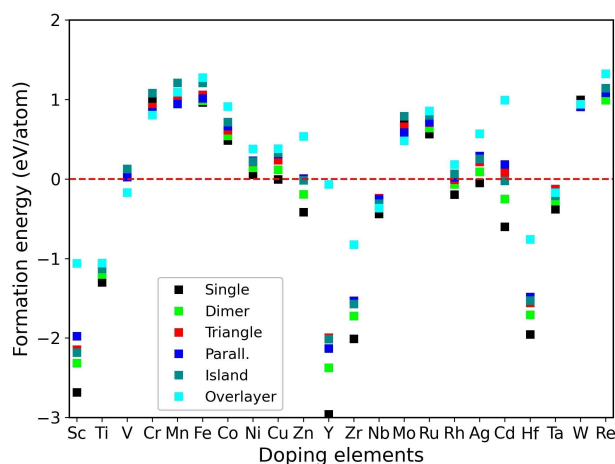
Results and Discussion

Before investigating transition metal element dopants, the pure PdH(111) surface is first studied by DFT with the BEEF–vdW functional. The crystal constants of optimized bulk PdH are $a = b = c = 4.138$ Å, which is well consistent with the experimental result of 4.090 Å.[40] Figure S1 shows the top and side view of pure PdH(111) structures. The PdH(111) slab is built by optimized bulk PdH and its lattice constants are $a = b = 8.778$ Å and $c = 27.140$ Å. The top and side views of pure PdH(111) with adsorbates HOCO*, CO*, H* and OH* are shown in Figure S2. We notice that HOCO*, CO* and OH* tend to adsorb on the top site of PdH, while H* prefers to adsorb on the hollow site according to their binding energies in Table S1. Figure S3 demonstrates the CO_2RR free energy diagram of PdH(111) at 0 V (vs. RHE), at room temperature. The free energies of the HOCO*, CO* and CO intermediates in this diagram are 0.820, 0.216 and 0.123 eV, respectively. Because the HOCO* formation step has the highest free energy, this reaction step is the potential-limiting step on pure PdH(111). This is consistent with the DFT results of 0.67 eV for the HOCO* step found by by Sheng et al. using the PW91 functional.[11] At the same time, the HER free energy diagram of PdH(111) at 0 V (vs. RHE) is also shown in Figure S4 and the free energy of the Volmer step is 0.501 eV, which is lower than 0.820 eV for CO_2RR. Therefore, the CO_2RR steps are thermodynamically more difficult than the HER steps for pure PdH. Experiments by Sheng et al. found that the CO/H_2 ratio is always lower than 1 at different potentials and thus show CO has a lower proportion, which has good agreement with computational results.[11]

In order to improve the CO2RR performance of PdH, the impact of doping transition metal elements into the PdH(111) surface is explored below. As displayed in Figure 1, we try to dope different elements Sc, Ti, V, Cr, Mn, Fe, Co, Ni, Cu, Zn, Y, Zr, Nb, Mo, Ru, Rh, Ag, Cd, Hf, Ta, W and Re into the PdH(111) surface in different doping configurations which we demote as: single, dimer, triangle, parallelogram, island and overlayer, respectively. Their formation energies per dopant atom in the different doping configurations is first calculated and shown in Table S2 and in Figure 2. We find, in most cases, that the overlayer doping is the most unstable, while single doping is the most stable when an element is doped in different
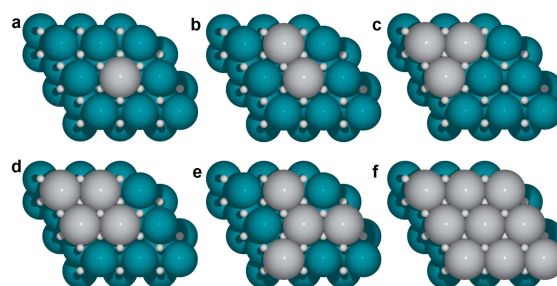

Figure 1. Top views of doping PdH(111) surface in different doping configurations: (a) single, (b) dimer, (c) triangle, (d) parallelogram, (e) island and (f) overlayer. The blue spheres are Pd atoms, the small white spheres represent H atoms and the grey spheres represent dopant atoms.

ChemSusChem

Research Article
doi.org/10.1002/cssc.202200008

**Chemistry
Europe**
European Chemical
Societies Publishing

Figure 2. Formation energies of doping PdH(111) with different elements in different doping configurations.

configurations. Moreover, the doping formation energies of Sc, Ti, Zn, Y, Zr, Nb, Hf and Ta in all doping configurations are negative except overlayer doping of Zn. This demonstrates that Sc, Ti, Zn, Y, Zr, Nb, Hf and Ta are easier to be doped into PdH compared to other elements. We note that for the largest dopants: Sc, Zn, Y, Zr, Ag, Cd, and Hf significant destabilization of the overlayer structure compared to single dopant by more than 1 eV can be observed. This is likely caused by the increased strain with the full overlayer.

The CO_2RR free energy diagrams of doping PdH(111) with different elements in different configurations are calculated to explore the possibility of lowering the potential-limiting HOCO* step as displayed in Figure 3. The free energies are calculated using the most stable adsorption sites according to the binding energies in Tables S3–S8 and the corresponding specific free energies are listed in Tables S11–S16 in the Supporting Information. For single atom doping of PdH(111), Fe, Zr, Nb and Ru doping effectively decrease the free energy of the HOCO* step by -0.003, -0.06, -0.07, and -0.15 eV, respectively, compared to the pure PdH. However, the doping formation energies of Fe and Ru are positive and thus unstable. Therefore, the candidates for lowering the HOCO* step are Nb and Zr doped PdH for doping with a single atom. For dimer doping of PdH(111), the free energies of HOCO* step of Sc, Ti, V, Cr, Mn, Fe, Y, Zr, Nb, Mo, Ru, Hf, Ta, W and Re are downhill relative to undoped PdH. Their free energy differences with respect to PdH are -0.39, -0.04, -0.01, -0.63, -0.30, -0.143, -0.88, -0.63, -0.04, -0.16, -0.19, -0.18, -0.10, -0.03, and -0.01 eV, respectively. Among them, Sc, Ti, Zr, Nb, Hf and Ta are stable according to their doping formation energies, and thus they are possible candidates for CO_2RR for this case. Doping with Y dimers is neglected due to structural distortion upon optimization. Still, for the triangle doping, Sc, Ti, V, Cr, Mn, Fe, Zr, Nb, Mo, Ru, Hf, Ta, W and Re doping leads to a free energy reduction of the potential-limiting step, and the free energy differences compared to pure PdH(111) are - 0.30, -0.17, -0.34, -0.57, -0.32, -0.30, -0.50, -0.24, -0.23, -0.21, -0.42, -0.41, -0.06 and -0.27 eV, respectively (Y doping is removed due to large structure distortion). The ones that could be stable are still
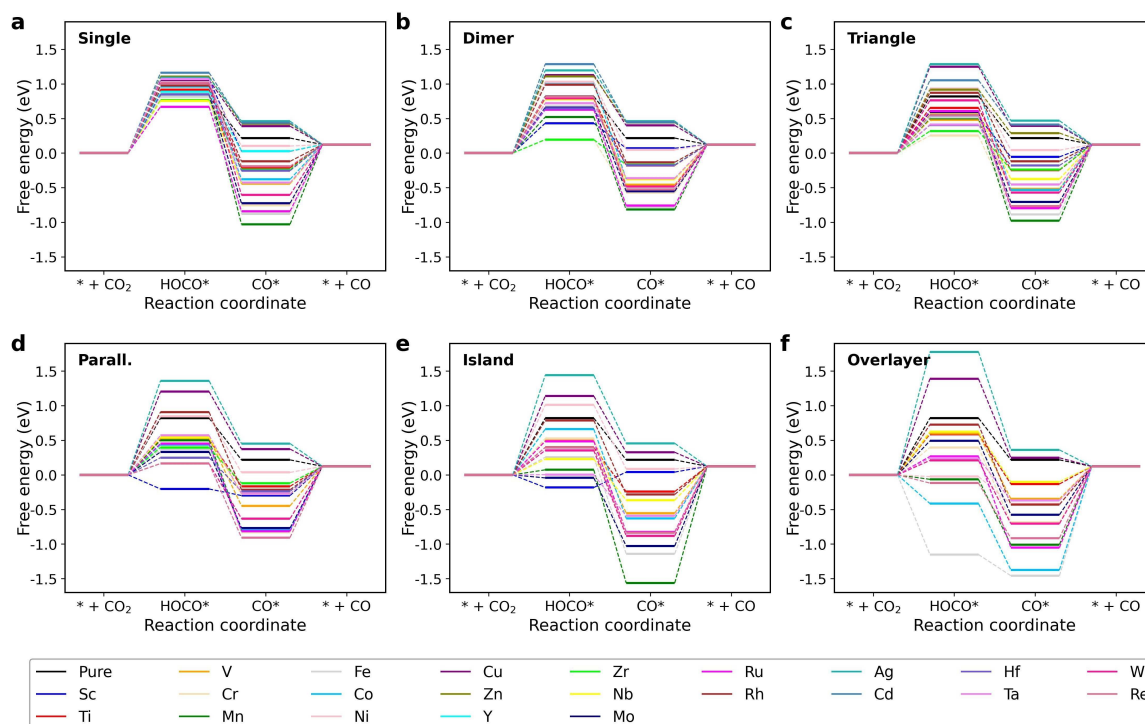
Figure 3. Free energy diagrams of doped PdH(111) with doping elements in different configurations.

Sc-, Ti-, Zr-, Nb-, Hf- and Ta-doped PdH. Similarly, there are more doping elements that can lower the potential-limiting step: Sc, Ti, V, Cr, Mn, Fe, Co, Zr, Nb, Mo, Ru, Hf, Ta, W and Re in the parallelogram configuration. Their free energy differences with respect to PdH are −1.02, −0.31, −0.29, −0.41, −0.32, −0.46, −0.39, −0.42, −0.28, −0.49, −0.37, −0.57, −0.25, −0.66, and −0.66 eV, respectively. In the parallelogram configuration Zn, Y and Cd doping are discarded due to large structural distortion. Again, the most promising stable candidates are Sc, Ti, Zr, Nb, Hf and Ta dopants. It is worth to notice that Sc doping in this case greatly decreases the HOCO* step and the line connecting HOCO* to CO* in the free energy diagram intersects with lines from other dopants. This illustrates that Sc doping clearly breaks the scaling relation between HOCO* and CO*. For the case of island doping, the free energies of Sc, Ti, V, Cr, Mn, Fe, Co, Nb, Mo, Ru, Rh, Ta, W and Re are downhill compared with that of the undoped PdH(111), and the free energy differences are −1.002, −0.423, −0.325, −0.293, −0.747, −0.565, −0.160, −0.592, −0.864, −0.333, −0.032, −0.817, −0.466 and −0.424 eV, respectively. Y, Zn, Zr, Cd and Hf doping are discarded due to large structure distortion in the island configuration. However, the stable dopants are Sc, Ti, Nb and Ta in the light of their negative formation energies. In the last configuration of overlayer doping, several structures are not stable after binding the reaction intermediates including Sc, Y, Zn, Zr, Cd and Hf overlayer surfaces. This may again be related to the large size of these dopants and the corresponding lattice mismatch that can be seen in Table S17, and thus they are removed in this case. Ti, V, Cr, Mn, Fe, Co, Ni, Nb, Mo, Ru, Rh, Ta, W and Re doping can effectively reduce the free energy of HOCO* step and the free energy differences are −0.232, −0.222, −0.423, −0.884, −1.971, −1.234, −0.844, −0.196, −0.329, −0.554, −0.093, −0.577, −0.611 and −0.939 eV, respectively, but only Ti, Nb, Ta and V doping are the stable ones. The candidates of different configurations for CO2RR are finally summarized in Table 1. Overall, we find that Ti, Sc, Nb, Zr, Hf and Ta doping of PdH(111) are promising dopant candidates in most configurations.

The scaling relations of intermediates on doped PdH(111) with different elements in different doping configurations are further studied to understand catalytic performance. Taking the top site adsorption as an example, the structures of the surface with HOCO*, CO*, H* and OH* are displayed in Figure 4a–d. The binding energies in the most stable sites are, however, applied in the following analysis with the corresponding data listed in Tables S3–S8. Figure 5 shows the scaling relation between HOCO* and CO* in the six dopant configurations. We use R^2, a
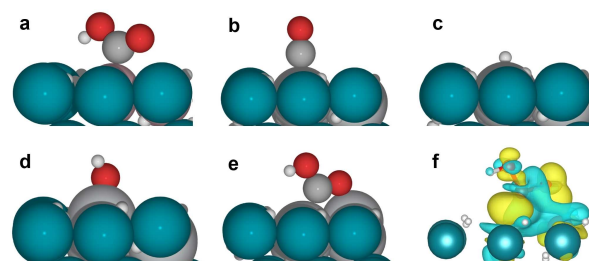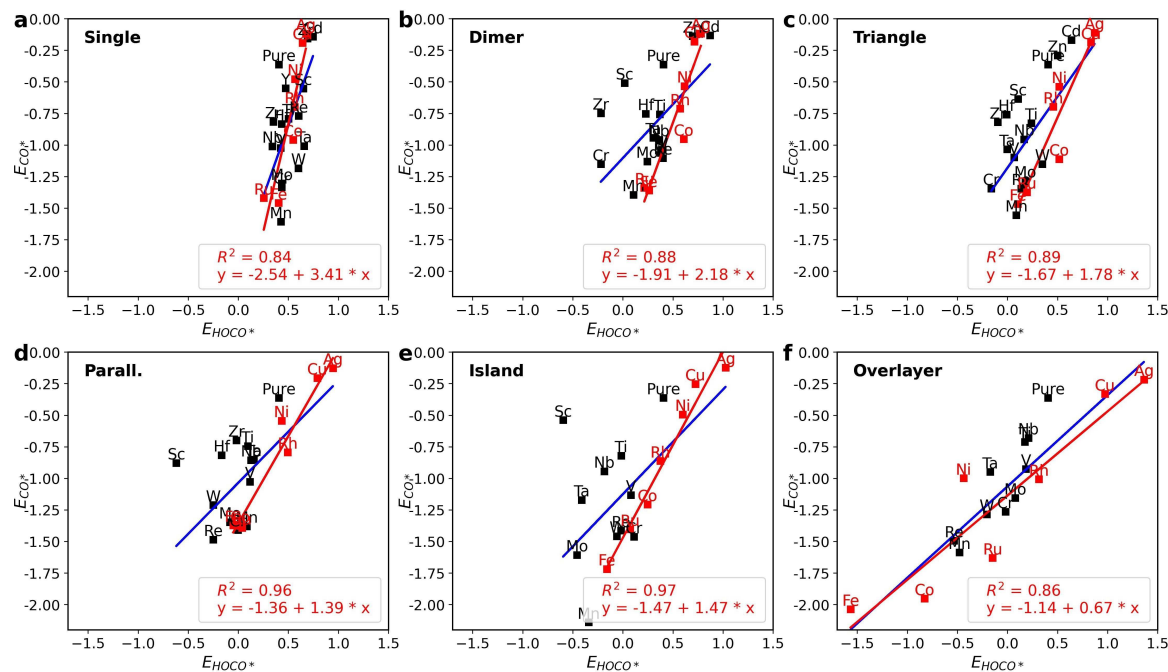
Figure 4. Structures of intermediates (a) HOCO* (one bond), (b) CO*, (c) H* and (d) OH* on the top sites of a doped PdH(111) surface. (e) HOCO* forms two bonds with PdH(111). The blue spheres are Pd atoms, the small white spheres represent H atoms, the big grey spheres represent dopant atoms, the red spheres are O atoms, and the small grey spheres are C atoms. (f) Charge density difference figure for HOCO* with two bonds. The blue region represents charge depletion while the yellow region means charge accumulation.

statistical measure that represents the proportion of the variance between two variables, to describe how well a linear scaling relation is fitted, and a good fit has R^2 close to 1. In Figure 5a–f, Fe, Co, Ni, Cu, Ru, Rh and Ag doping are marked in red dots and the corresponding fitted lines are also shown in red. They display clear linear scaling relations in all configurations with R^2 values 0.84, 0.88, 0.89, 0.96, 0.97 and 0.86, respectively. This is because they all form only a C–metal bond on the top of one dopant in all doping configurations according to optimized HOCO* structures as shown in Figure 4a. The fitted lines of the six doping cases using all doping elements are displayed by the blue lines. They show much lower R^2 values of 0.42, 0.36, 0.51, 0.48, 0.41, and 0.80, respectively. This is because the surfaces doped with Sc, Ti, Nb, Zr, Zn, V, Mn, Mo, Cr, Hf, Cd, W, Ta, and Re mostly tend to form two bonds to the surface consisting of a C–Metal (C–M) and an O–Metal (O–M) on two different metal atoms for HOCO* on the surface as displayed in Figure 4e. A small part of them, however, forms two bonds to the same metal atom as shown in Figure S11. All structures are summarized in the database in the supporting information and the corresponding formation of two bonds can be found in the database. The C–M and O–M bond lengths of HOCO* on the doped surfaces in different configurations are listed in Tables S18 and S19, and O–M bond lengths are summarized in figure S15. We have chosen a surface-oxygen distance of 2.7 Å to determine whether a bond is formed between the O in HOCO and the surface because few surfaces have O–M bond lengths between 2.4 and 2.8 Å. A more detailed discussion is given in the supporting information. For example, Figure 4f shows the charge density difference for HOCO* on the Ti parallelogram doped surface, which clearly demonstrates that two bonds form to the surface. The bond length of C–Ti is 2.259 Å and the bond length of O–Ti is 2.032 Å. We therefore conclude the formation of two bonds breaks the previous single C–Metal scaling relations and thus reduces the R^2. Furthermore, the dopant structures resulting in the formation of two bonds show stronger HOCO* binding with the surface compared to their CO* binding energy, which may be the reason the free energies of the HOCO* step with the two bonds are relatively

Table 1. Possible candidates for different PdH(111) doping configurations according to free energy diagrams.

Doping configurations	Possible candidates
single	Nb, Zr
dimer	Sc, Ti, Nb, Zr, Hf, Ta
triangle	Sc, Ti, Nb, Zr, Hf, Ta
parallelogram	Sc, Ti, Nb, Zr, Hf, Ta
island	Sc, Ti, Nb, Ta
overlayer	Ti, Nb, Ta, V

ChemSusChem

Research Article
doi.org/10.1002/cssc.202200008

Chemistry Europe
European Chemical
Societies Publishing

Figure 5. Scaling relation of intermediates on doped PdH(111) with different elements between HOCO* and CO* in different dopant configurations. The red line is fitted to Fe, Co, Ni, Cu, Ru, Rh and Ag doped PdH(111) where HOCO* forms one bond to the surface. The blue line is fitted to all doped PdH(111).

low in Figure 3. Figure S12 shows the scaling relations of adsorbates HOCO* vs. OH* in different doping configurations. Similarly, for the surfaces doped with Fe, Co, Ni, Cu, Ru, Rh, and Ag, their HOCO* binding energies can scale linearly with the OH* energies, and the R^2 values are 0.81, 0.82, 0.81, 0.63, 0.77 and 0.83 in different doping configurations, respectively. However, their scaling relations of total metal element doped surfaces have worse R^2 values of 0.03, 0.46, 0.62, 0.60, 0.80, 0.50, respectively. This could also be attributed to the formation of the two bonds of HOCO* on the surfaces as we described before. The scaling relations between CO* and H* intermediates on doped PdH(111) surfaces in different doping configurations are also shown in Figure S13. The CO* and H* intermediates display good scaling relations with R^2 values of 0.68, 0.80, 0.74, 0.66, 0.78 and 0.49. This can be attributed to the fact that only one atom in CO* and H* interacts with the surfaces.

In order to further study the kinetic activity of doped PdH(111), a kinetic model is utilized. In Figure 6, the activity volcano of doped PdH(111) for CO_2RR in different doping configurations are given. It is seen that the kinetic activities depend on the binding energies of both HOCO* and CO*. The partial pressure of CO_2 and CO are 101325 Pa and 5562 Pa, respectively, and the overpotential (the difference between the applied potential and the equilibrium potential calculated with the BEEF–vdW functional) is set to 0.3 V. It can be noted that Ti, Sc, Nb and Zr demonstrate excellent catalytic activities in different doping configurations. Among them, Sc doping with dimer, triangle and island configurations, Zr doping with dimer, triangle and parallelogram configurations and Hf doping with dimer, triangle and parallelogram configuration are close to the center of the volcano and thus show good activities. However,

according to binding energy in Figure S12, OH* binding of Sc, Zr and Hf are so strong on the PdH surface, which will cause OH* poisoning. Besides, we notice that Ti doping with parallelogram and overlayer configuration and Nb doping with overlayer configuration are also closer to the center of the volcano compared to PdH. Furthermore, the free energies of OH* are smaller than 0.3 eV and thus will not be poisoned at 0.3 V overpotential. Therefore, they are expected to have better kinetic activities than pure surface. However, we can find that CO* binding of Ti and Nb doping are stronger than pure PdH, which limits their kinetic activities at room temperature due to slow CO desorption. In order to further improve CO* activities of noneletrochemical step, one could increase the temperature. As shown in Figure S14, we take Ti doping in the parallelogram configuration as an example. With the temperature increasing, the partial current density of CO* would increase and 7.72 mA cm^{-2} can be achieved at 350 K. In addition, we calculate the surface stability and the corresponding Pourbaix diagram[41,42] of HOCO*, CO*, H*, OH*, metal ion dissolution, for PdH(111) surfaces including Ti doping in parallelogram and overlayer configurations, Nb doping with overlayer configurations, and pure PdH(111) as displayed in Figures S20–S25. The detailed methods are given in the supporting information. It is noticed that ion dissolution is unfavorable when the potential is less than or equal to −0.304, −0.290, −0.224 and 1.017 V at pH = 0 for these four configurations, and the dissolution potential will be more negative as pH increases. This means that these three doped surfaces are stable under negative bias typically required for CO_2 reduction, but that stability might be an issue above the working potential.
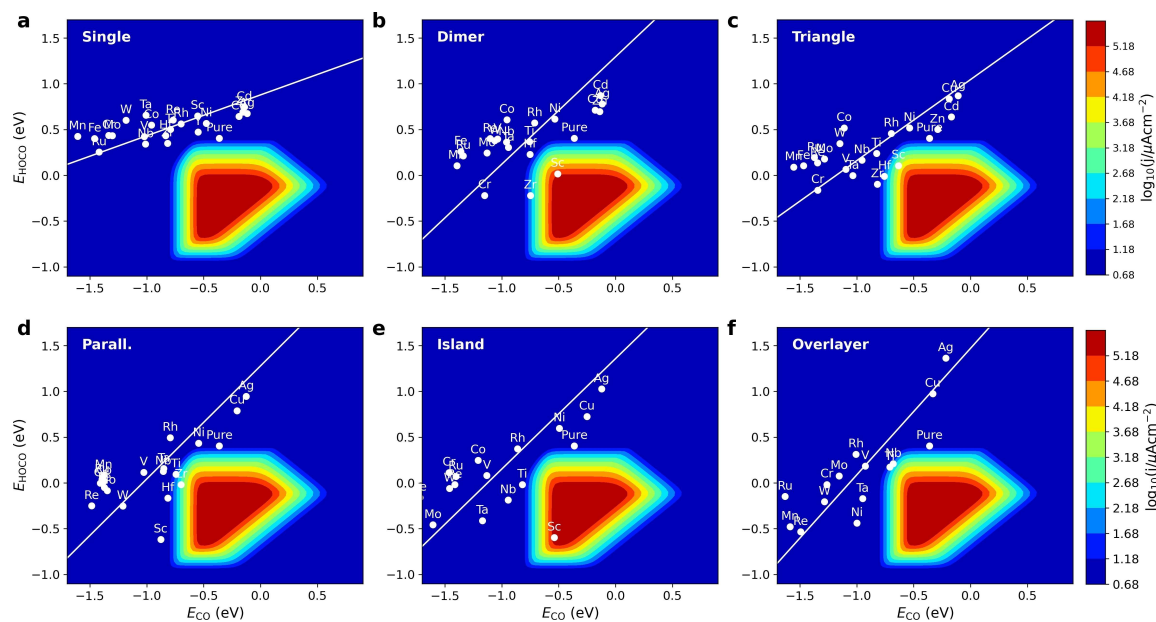
Figure 6. Activity volcano plots of doped PdH(111) with different elements for CO_2RR at 0.3 V overpotential in different dopant configurations.

Figure 7 illustrates the selectivity for CO2RR and HER of doped PdH(111) in different doping configurations with the corresponding data listed in Tables S3–S8. We apply $\Delta G_{HOCO*}-\Delta G_{H*}$ as a descriptor to demonstrate the trend of producing CO_2 and H_2. When the value of $\Delta G_{HOCO*}-\Delta G_{H*}$ is more negative, it indicates that there would be higher selectivity toward CO_2RR. Otherwise, the more positive value of $\Delta G_{HOCO*}-\Delta G_{H*}$ represents the higher selectivity toward HER. We find that a majority of elements doped PdH in different doping configuration will generate more H_2 than CO according to Figure 7. However, some overlayer doping such as, Sc, Mn, Fe, Co, Ni and Zr prefer to generate more CO. It is worth noting that the values for Ti and Nb doping are more negative than for pure PdH(111) in

most doping configurations and thus tend to produce more CO.

Conclusions

Density functional theory calculations have been applied to study the CO_2RR and the competing HER of PdH(111). 22 transition metal elements Sc, Ti, V, Cr, Mn, Fe, Co, Ni, Cu, Zn, Y, Zr, Nb, Mo, Ru, Rh, Ag, Cd, Hf, Ta, W and Re are doped into the PdH(111) surface in different doping configurations to explore their catalytic performance. Doping formation energies show Sc, Ti, Zn, Y, Zr, Nb, Hf and Ta dopants are easier to dope into the surface. Free energy diagrams identify Ti, Sc, Nb, Zr, Hf and Ta as possible doping candidates which lower the HOCO* limiting step for the CO_2RR. The scaling relations of HOCO* vs. CO* binding energies in different doping configurations display well-defined scaling relations for Fe, Co, Ni, Cu, Ru, Rh and Ag doping because HOCO* and CO* intermediates all form a single C–Metal on the surfaces. However, the formation of the two bonds consisting of one C–Metal and one O–Metal bond break the scaling relation for other dopants, which is the reason why these dopants have strong HOCO* binding compared to the CO* binding. According to kinetic volcano plots, Ti doping with parallelogram and overlayer configuration and Nb doping with overlayer configuration are further found to have better kinetic activities than pure PdH(111) at a low overpotential of 0.3 V. At the same time, Ti and Nb are also possible to generate more CO compared with pure surface based on their selectivity toward the CO_2RR and HER.
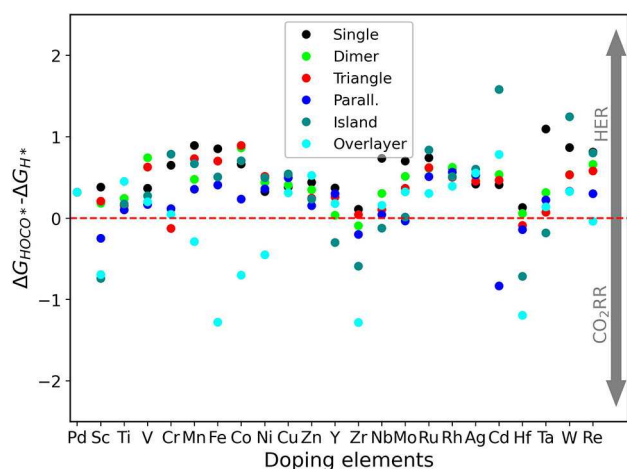
Figure 7. Selectivity plot for CO_2RR and HER of doped PdH(111) with elements in different dopant configurations.

Acknowledgements

Conflict of Interest

The authors declare no conflict of interest.

Data Availability Statement

The data that support the findings of this study are openly available in DTU Data Repository at https://doi.org/10.11583/DTU.17263532, reference number 17263532.

[1] S. Nitopi, E. Bertheussen, S. B. Scott, X. Liu, A. K. Engstfeld, S. Horch, B. Seger, I. E. L. Stephens, K. Chan, C. Hahn, J. K. Nørskov, T. F. Jaramillo, I. Chorkendorff, *Chem. Rev.* **2019**, *119*, 7610–7672.

[2] J. E. Szulejko, P. Kumar, A. Deep, K.-H. Kim, *Atmos. Pollut. Res.* **2017**, *8*, 136–140.

[3] G. Centi, S. Perathoner, *Catal. Today* **2009**, *148*, 191–205.

[4] L. Fan, C. Xia, P. Zhu, Y. Lu, H. Wang, *Nat. Commun.* **2020**, *11*.

[5] Q. He, J. H. Lee, D. Liu, Y. Liu, Z. Lin, Z. Xie, S. Hwang, S. Kattel, L. Song, J. G. Chen, *Adv. Funct. Mater.* **2020**, *30*, 2000407.

[6] M. Umeda, Y. Niitsuma, T. Horikawa, S. Matsuda, M. Osawa, *ACS Appl. Energ. Mater.* **2019**, *3*, 1119–1127.

[7] Y. Huo, X. Peng, X. Liu, H. Li, J. Luo, *ACS Appl. Mater. Interfaces* **2018**, *10*, 12618–12625.

[8] K. U. D. Calvinho, A. B. Laursen, K. M. K. Yap, T. A. Goetjen, S. Hwang, N. Murali, B. Mejia-Sosa, A. Lubarski, K. M. Teeluck, E. S. Hall, E. Garfunkel, M. Greenblatt, G. C. Dismukes, *Energy Environ. Sci.* **2018**, *11*, 2550–2559.

[9] E. Bertheussen, A. Verdaguer-Casadevall, D. Ravasio, J. H. Montoya, D. B. Trimarco, C. Roy, S. Meier, J. Wendland, J. K. Nørskov, I. E. L. Stephens, I. Chorkendorff, *Angew. Chem.* **2015**, *128*, 1472–1476.

[10] S. Wang, T. Kou, S. E. Baker, E. B. Duoss, Y. Li, *Adv. Energy Sustainability Res.* **2021**, 2100131.

[11] W. Sheng, S. Kattel, S. Yao, B. Yan, Z. Liang, C. J. Hawxhurst, Q. Wu, J. G. Chen, *Energy Environ. Sci.* **2017**, *10*, 1180–1185.

[12] I. Wender, *Fuel Process. Technol.* **1996**, *48*, 189–297.

[13] E. R. Cave, J. H. Montoya, K. P. Kuhl, D. N. Abram, T. Hatsukade, C. Shi, C. Hahn, J. K. Nørskov, T. F. Jaramillo, *Phys. Chem. Chem. Phys.* **2017**, *19*, 15856–15863.

[14] R. Shi, J. Guo, X. Zhang, G. I. N. Waterhouse, Z. Han, Y. Zhao, L. Shang, C. Zhou, L. Jiang, T. Zhang, *Nat. Commun.* **2020**, *11*.

[15] S. A. Mahyoub, F. A. Qaraah, C. Chen, F. Zhang, S. Yan, Z. Cheng, *Sustain. Energy Fuels* **2020**, *4*, 50–67.

[16] C. Kim, H. S. Jeon, T. Eom, M. S. Jee, H. Kim, C. M. Friend, B. K. Min, Y. J. Hwang, *J. Am. Chem. Soc.* **2015**, *137*, 13844–13850.

[17] D. Raciti, K. J. Livi, C. Wang, *Nano Lett.* **2015**, *15*, 6829–6835.

[18] Y. Chen, C. W. Li, M. W. Kanan, *J. Am. Chem. Soc.* **2012**, *134*, 19969–19972.

[19] W. Zhu, S. Kattel, F. Jiao, J. G. Chen, *Adv. Energy Mater.* **2019**, *9*, 1802840.

[20] L. Delafontaine, T. Asset, P. Atanassov, *ChemSusChem* **2020**, *13*, 1688–1698.

[21] D. Gao, H. Zhou, J. Wang, S. Miao, F. Yang, G. Wang, J. Wang, X. Bao, *J. Am. Chem. Soc.* **2015**, *137*, 4288–4291.

[22] J. H. Lee, S. Kattel, Z. Jiang, Z. Xie, S. Yao, B. M. Tackett, W. Xu, N. S. Marinkovic, J. G. Chen, *Nat. Commun.* **2019**, *10*.

[23] G. Kresse, J. Hafner, *Phys. Rev. B* **1993**, *47*, 558–561.

[24] G. Kresse, J. Hafner, *Phys. Rev. B* **1994**, *49*, 14251–14269.

[25] G. Kresse, J. Furthmüller, *Comput. Mater. Sci.* **1996**, *6*, 15–50.

[26] G. Kresse, J. Furthmüller, *Phys. Rev. B* **1996**, *54*, 11169–11186.

[27] A. H. Larsen, J. J. Mortensen, J. Blomqvist, I. E. Castelli, R. Christensen, M. Du lak, J. Friis, M. N. Groves, B. Hammer, C. Hargus, E. D. Hermes, P. C. Jennings, P. B. Jensen, J. Kermode, J. R. Kitchin, E. L. Kolsbjerg, J. Kubal, K. Kaasbjerg, S. Lysgaard, J. B. Maronsson, T. Maxson, T. Olsen, L. Pastewka, A. Peterson, C. Rostgaard, J. Schiøtz, O. Schütt, M. Strange, K. S. Thygesen, T. Vegge, L. Vilhelmsen, M. Walter, Z. Zeng, K. W. Jacobsen, *J. Phys. Condens. Matter* **2017**, *29*, 273002.

[28] S. Bahn, K. Jacobsen, *Comput. Sci. Eng.* **2002**, *4*, 56–66.

[29] J. Wellendorff, K. T. Lundgaard, A. Møgelhøj, V. Petzold, D. D. Landis, J. K. Nørskov, T. Bligaard, K. W. Jacobsen, *Phys. Rev. B* **2012**, *85*.

[30] P. E. Blöchl, *Phys. Rev. B* **1994**, *50*, 17953–17979.

[31] C. Ai, T. Vegge, H. A. Hansen, Metal-doped PdH(111) Database, https://doi.org/10.11583/DTU.17263532.

[32] H. J. Monkhorst, J. D. Pack, *Phys. Rev. B* **1976**, *13*, 5188–5192.

[33] R. Christensen, H. A. Hansen, T. Vegge, *Catal. Sci. Technol.* **2015**, *5*, 4946–4949.

[34] A. Bhowmik, H. A. Hansen, T. Vegge, *ACS Catal.* **2017**, *7*, 8502–8513.

[35] A. A. Peterson, F. Abild-Pedersen, F. Studt, J. Rossmeisl, J. K. Nørskov, *Energy Environ. Sci.* **2010**, *3*, 1311.

[36] J. K. Nørskov, J. Rossmeisl, A. Logadottir, L. Lindqvist, J. R. Kitchin, T. Bligaard, H. J'onsson, *J. Phys. Chem. B* **2004**, *108*, 17886–17892.

[37] Y. Hori, A. Murata, R. Takahashi, *J. Chem. Soc. Faraday Trans. 1* **1989**, *85*, 2309.

[38] J. K. Nørskov, T. Bligaard, A. Logadottir, J. R. Kitchin, J. G. Chen, S. Pandelov, U. Stimming, *J. Electrochem. Soc.* **2005**, *152*, J23.

[39] H. A. Hansen, J. B. Varley, A. A. Peterson, J. K. Nørskov, *J. Phys. Chem. Lett.* **2013**, *4*, 388–392.

[40] J. E. Schirber, B. Morosin, *Phys. Rev. B* **1975**, *12*, 117–118.

[41] T. Patniboon, H. A. Hansen, *ACS Catal.* **2021**, *11*, 13102–13118.

[42] H. A. Hansen, J. Rossmeisl, J. K. Nørskov, *Phys. Chem. Chem. Phys.* **2008**, *10*, 3722.